


Dimensionality crossover for moiré excitons in twisted bilayers of anisotropic two-dimensional semiconductors

Isaac Soltero^{1,2,3} and David A. Ruiz-Tijerina^{1,*}

¹*Departamento de Física Química, Instituto de Física, Universidad Nacional Autónoma de México, Ciudad de México, C.P. 04510, México*

²*Department of Physics and Astronomy, University of Manchester, Booth St. E., Manchester M13 9PL, United Kingdom*

³*National Graphene Institute, University of Manchester, Booth St. E., Manchester M13 9PL, United Kingdom*

 (Received 7 August 2023; revised 18 October 2023; accepted 19 October 2023; published 6 November 2023)

We study the energies and optical spectra of excitons in twisted bilayers of anisotropic van der Waals semiconductors exhibiting moiré patterns, taking phosphorene as a case study. Leveraging the scale separation between the moiré length scale and the exciton Bohr radii, we introduce a continuous model for Wannier excitons that incorporates the spatial variation of their binding energies. Our calculations reveal a dimensionality crossover for the exciton states, driven by the combined dispersion and moiré potential anisotropies, from quantum dot lattices at twist angles $\theta < \theta_*$, to quantum wire arrays at $\theta > \theta_*$, with crossover angle $\theta_* = 4^\circ$. We identify clear signatures of this dimensionality crossover in the twist angle dependence of the excitonic absorption spectra, which allows experimental verification of our theoretical results through standard optical measurements. Our results establish two-dimensional anisotropic moiré semiconductors as versatile solid-state platforms for exploring bosonic correlations across different dimensionalities.

DOI: [10.1103/PhysRevB.108.L201401](https://doi.org/10.1103/PhysRevB.108.L201401)

Introduction. Moiré heterostructures of two-dimensional (2D) semiconductors have recently emerged as solid-state quantum simulators [1], exhibiting multiple strongly correlated states of fermionic [2–5], bosonic [6,7], and mixed Fermi-Bose [8] matter. Heterostructures based on hexagonal crystals, such as transition-metal dichalcogenides (TMDs), are known to realize generalized Hubbard models for charge carriers and excitons [9–11], where strong correlations arise due to large on-site interaction to tunneling ratios between neighboring superlattice sites, controlled by the twist angle. More recently, anisotropic moiré semiconductors with rectangular unit cells have been predicted [12–14] and experimentally verified [5] to host electronic Tomonaga-Luttinger liquids. In these materials, including phosphorene, group-IV monochalcogenides (e.g., GeSe and SnSe), and $1T'$ -phase TMDs, the moiré superlattice strongly amplifies the structural and band anisotropies, resulting in one-dimensional (1D) conduction and valence states with quantum-wire-like spatial profiles, where correlations arise due to the strong lateral confinement [15]. Crossovers from this Tomonaga-Luttinger regime into both an anisotropic Hubbard and a 2D dispersive regime are possible by decreasing and increasing the interlayer twist angle, respectively [14,16], making moiré anisotropic semiconductors promising platforms for exploring strong correlations between zero-, one-, and two-dimensional fermions. However, the effects of these dimensionality crossovers remain unexplored in the case of the ubiquitous bosonic quasiparticle arising in 2D semiconductors: the exciton.

In this Letter, twisted bilayers of anisotropic 2D semiconductors are established as versatile platforms for exploring excitonic physics across dimensionalities. Taking twisted bilayer phosphorene as a case study, we introduce a fully parametrized continuous Hamiltonian for Wannier excitons in the resulting moiré superlattice (mSL), based on our model for carriers of Ref. [14], and which relies only on a clear scale separation between the excitonic Bohr radii and the moiré wavelength. Numerical solution of our model reveals a dimensionality crossover [17,18] for the low-energy excitons, going from quantum-dot-like states for twist angles $\theta < \theta_*$ to quantum-wire-like states for $\theta > \theta_*$, with a theoretical crossover angle $\theta_* = 4^\circ$. We expect that our results can be extended to excitons in moiré heterostructures of group-IV monochalcogenides, which are isoelectronic [19] with, and structurally similar to phosphorene.

Model. Phosphorene, a single layer of black phosphorus, is a direct-gap 2D semiconductor known for its strongly anisotropic dispersion, high carrier mobility, and strong linear optical dichroism [20]. Structurally, phosphorene has a puckered structure, with a four-atom rectangular unit cell described by the C_{2h} point symmetry group [21] [Fig. 1(a)], with estimated lattice constants [14] $a_x = 3.296 \text{ \AA}$ and $a_y = 4.590 \text{ \AA}$. Its conduction- and valence-band extrema occur at the Γ point of the Brillouin zone, with Bloch states that transform as the B_u and A_g irreducible representations of group C_{2h} , respectively. This is in stark contrast with TMDs, whose band extrema occur at the $\pm\mathbf{K}$ valleys, thus introducing a momentum mismatch between valley carriers in twisted structures [22,23]. Thus far, the use of phosphorene in twistronics has been hindered by its low stability in air and water [24], which requires the use of inert atmospheres and special dry-transfer techniques [25]. Nonetheless, recent successes in the

*d.ruiz-tijerina@fisica.unam.mx

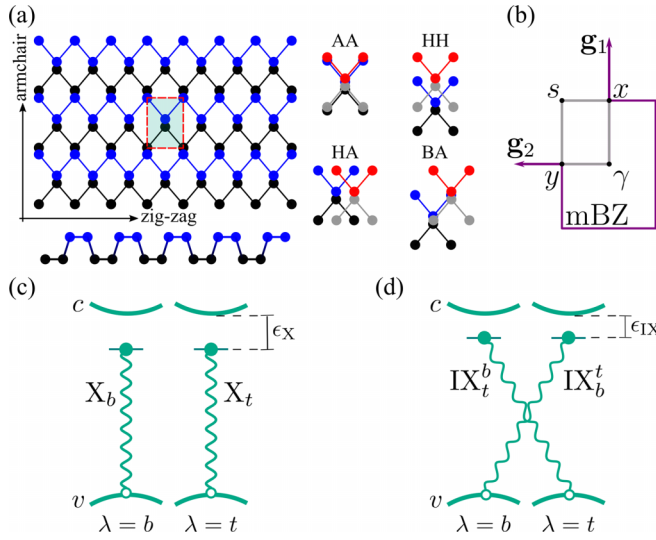


FIG. 1. (a) Top and side views of the phosphorene crystal structure, with its zigzag (armchair) direction along the $\hat{\mathbf{x}}$ ($\hat{\mathbf{y}}$) axis. The unit cell is marked by the red, dashed rectangle. The four high-symmetry registries of bilayer phosphorene are shown on the right. (b) Moiré Bragg vectors and the corresponding moiré Brillouin zone (mBZ). Symmetry points are labeled as γ , x , s , and y . (c) Schematic of the two possible intra- and (d) interlayer excitons. Electrons (holes) are indicated by a solid (empty) circle. Wavy lines indicate the electrostatic interaction binding the electron-hole pair, with a binding energy ϵ_X or ϵ_{IX} .

fabrication of twisted structures [25–27] suggest that phosphorene- and group-IV monochalcogenide-based [28] twistronics may now be possible.

We consider the moiré pattern formed in a phosphorene bilayer with a small relative twist angle $\theta \lesssim 6^\circ$ and large moiré supercell (mSC) containing more than 100 atomic unit cells. Every region in the mSC, centered at some position \mathbf{r} along the sample plane, is locally described by its approximate commensurate stacking, fully defined by an in-plane offset vector $\mathbf{r}_0(\mathbf{r})$ and the local interlayer distance $d[\mathbf{r}_0(\mathbf{r})]$. The primitive Bragg vectors of the mSL are

$$\mathbf{g}_1 \approx \frac{2\pi\theta}{a_x} \hat{\mathbf{y}}, \quad \mathbf{g}_2 \approx -\frac{2\pi\theta}{a_y} \hat{\mathbf{x}}, \quad (1)$$

and define the moiré Brillouin zone (mBZ) shown in Fig. 1(b). The corresponding mSL basis vectors are

$$\mathbf{a}_1^M \approx \frac{a_x}{\theta} \hat{\mathbf{y}}, \quad \mathbf{a}_2^M \approx -\frac{a_y}{\theta} \hat{\mathbf{x}}. \quad (2)$$

To study the exciton states of the twisted bilayer, we start from the continuous moiré potential model for Γ -point conduction (c) and valence (v) electrons introduced in Ref. [14]:

$$H_m = \sum_{\alpha,\lambda} \int d^2r \epsilon_\alpha^\lambda(\mathbf{r}) \varphi_{\alpha\lambda}^\dagger(\mathbf{r}) \varphi_{\alpha\lambda}(\mathbf{r}) + \sum_\alpha \int d^2r [T_\alpha(\mathbf{r}) \varphi_{\alpha t}^\dagger(\mathbf{r}) \varphi_{\alpha b}(\mathbf{r}) + \text{H.c.}], \quad (3)$$

with $\varphi_{\alpha\lambda}(\mathbf{r})$ the electron field operator for band $\alpha = c, v$ in layer $\lambda = t, b$ (for top and bottom, respectively) at position \mathbf{r} . The position-dependent state energies $\epsilon_\alpha^\lambda(\mathbf{r})$ and tunneling

TABLE I. Binding energy interpolation parameters in Eq. (5) for intra- (X) and interlayer (IX) excitons. All parameters are reported in meV.

n	X		IX	
	$\epsilon_{X,n}^s$	$\epsilon_{X,n}^a$	$\epsilon_{IX,n}^s$	$\epsilon_{IX,n}^a$
1	0.050	0.759	-0.089	0.112
2	0.991	1.120	-1.430	-1.607
3	-0.674	0.204	0.913	0.293
4	-0.638	0.681	0.972	-0.349
$\epsilon_{X,0} = -209.392$			$\epsilon_{IX,0} = -107.833$	

energies $T_\alpha(\mathbf{r})$ have the mSL periodicity, and as such are expressed as Fourier series over the mSL reciprocal vectors $\mathbf{g}_{m,n} = m\mathbf{g}_1 + n\mathbf{g}_2$, with m, n integers [29].

We then evaluate the matrix elements of the moiré potential (3) between the different exciton states of interest that can be formed in the four-band system. We identify two types of intralayer excitons (X)—one for each monolayer—and two types of interlayer excitons (IX), shown schematically in Figs. 1(c) and 1(d), with two-body wave functions

$$|X_{\lambda,n}(\mathbf{Q})\rangle = \int d^2r \frac{e^{i\mathbf{Q}\cdot\mathbf{r}}}{\sqrt{S}} \int d^2\rho X_n(\rho) \times \varphi_{c\lambda}^\dagger(\mathbf{r}_e[\rho, \mathbf{r}]) \varphi_{v\lambda}(\mathbf{r}_h[\rho, \mathbf{r}]) |\Omega\rangle, \quad (4a)$$

$$|IX_{\lambda,\bar{\lambda},n}(\mathbf{Q})\rangle = \int d^2r \frac{e^{i\mathbf{Q}\cdot\mathbf{r}}}{\sqrt{S}} \int d^2\rho Y_n(\rho) \times \varphi_{c\lambda}^\dagger(\mathbf{r}_e[\rho, \mathbf{r}]) \varphi_{v\bar{\lambda}}(\mathbf{r}_h[\rho, \mathbf{r}]) |\Omega\rangle. \quad (4b)$$

Here, $|X_{\lambda,n}(\mathbf{Q})\rangle$ represents an intralayer exciton with relative motion (RM) quantum numbers n , and center of mass (c.m.) wave vector \mathbf{Q} in layer λ ; and $|IX_{\lambda,\bar{\lambda},n}(\mathbf{Q})\rangle$ an interlayer exciton formed by a λ -layer hole, and an electron in the opposite layer $\bar{\lambda}$. \mathbf{r} and ρ are the c.m. and RM position vectors, respectively; $X_n(\rho)$ and $Y_n(\rho)$ are the corresponding electron-hole RM wave functions; $|\Omega\rangle$ represents the phosphorene charge-neutral ground state, with a full (empty) valence (conduction) band; and S is the sample surface area.

The exciton binding energies and RM wave functions are described by the anisotropic Wannier equation, with a screened interaction corresponding to a bilayer immersed in a medium with dielectric tensor [30] $\epsilon = \text{diag}(\epsilon_{\parallel}, \epsilon_{\perp}, \epsilon_{\perp})$. Given its experimental relevance, we consider hexagonal boron nitride (hBN) encapsulation, using its high-frequency dielectric constants [31] $\epsilon_{\parallel} = 5$, $\epsilon_{\perp} = 3$ [32,33]). Interactions in the bilayer depend on the interlayer distance [34,35] $d[\mathbf{r}_0(\mathbf{r})]$, which varies spatially according to the local stacking $\mathbf{r}_0(\mathbf{r})$ [Fig. 2(a)], making the binding energies and RM wave functions position dependent within the continuous approximation. As the stacking vector $\mathbf{r}_0(\mathbf{r})$ varies slowly across the moiré supercell over length scales of the order of the moiré periodicity, so does the interlayer distance. By comparison, the excitonic RM wave-function extension is only $\sim 10 \text{ \AA}$ [36]. This clear scale separation allows us to treat the exciton binding energies as adiabatic functions of position, effectively

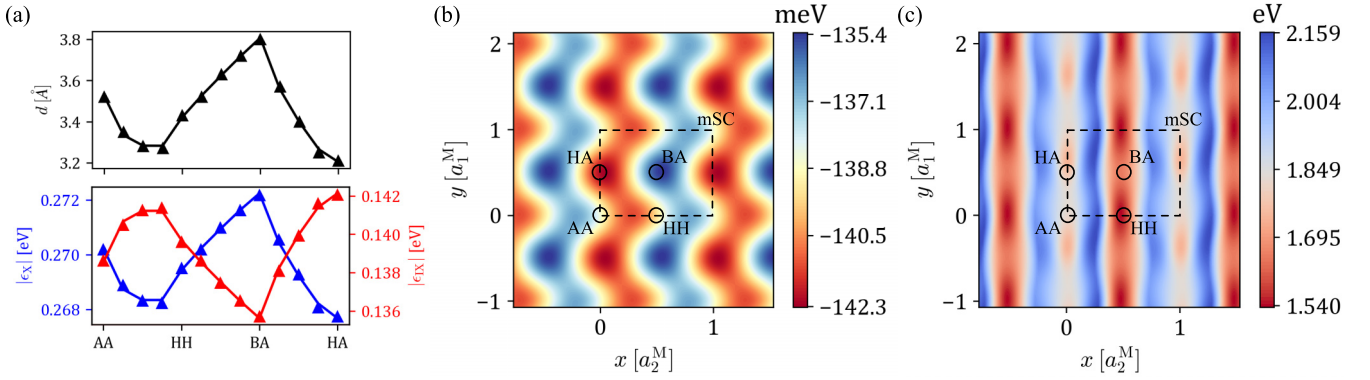


FIG. 2. (a) Interlayer distance d (top) and absolute value of exciton binding energies $|\epsilon|$ (bottom) at 13 different stacking configurations across the mSC, including the high-symmetry points AA, HH, BA, and HA. For both intralayer (ϵ_X , blue) and interlayer (ϵ_{IX} , red) binding energies the fitting function (5) is shown as solid lines with parameters shown in Table I. (b) Interlayer exciton binding energy as a function of position for the twisted phosphorene bilayer resulting from the interpolation (5). (c) Effective moiré potential for excitons, where potential wells are formed at the HH mSL regions. For both (b) and (c), x and y axes are scaled with respect to the superlattice parameters a_2^M and a_1^M , respectively. The mSC and high-symmetry regions are labeled.

representing scalar potentials for intra- and interlayer excitons [37], $\epsilon_X(\mathbf{r})$ and $\epsilon_{IX}(\mathbf{r})$, respectively.

The moiré pattern contains four high-symmetry stacking configurations, labeled AA, HH, HA, and BA in Figs. 1(a) and 2. We have solved the anisotropic Wannier equation locally at these four, and nine other intermediate regions of the mSC [29], using a semianalytical direct diagonalization method [38] that has proven successful for studying excitons in 2D semiconductors [35,36,39,40]. The calculated local binding energies across the mSC are reported in Fig. 2(a), along with the corresponding interlayer distances, from Ref. [14]. Whereas a Rydberg-like sequence is obtained for each local registry, here we focus only on the lowest X and IX states, henceforth called $1s$ excitons [41]. Figure 2(a) shows opposite trends for the X and IX binding energies as functions of the interlayer distance, explained as follows: the screening by layer $\bar{\lambda}$ of the electron-hole interaction in layer λ is reduced as d increases, leading to a larger $|\epsilon_X|$. By contrast, a larger d increases the electron-hole separation in an IX state, in detriment of the interlayer interaction, thus reducing $|\epsilon_{IX}|$. The scalar potentials $\epsilon_\mu(\mathbf{r})$ ($\mu = X, IX$) are obtained by interpolating the stacking dependence of the binding energies as

$$\epsilon_\mu(\mathbf{r}) = \epsilon_{\mu,0} + \sum_{n=1}^4 [\epsilon_{\mu,n}^s \cos(\mathbf{g}_n \cdot \mathbf{r}) + \epsilon_{\mu,n}^a \sin(\mathbf{g}_n \cdot \mathbf{r})], \quad (5)$$

with the fitting parameters of Table I [solid lines in Fig. 2(a)]. The spatial variation of the extrapolated IX binding energy (5) across the moiré superlattice is shown in Fig. 2(b).

Computing the matrix elements of (3), including (5), in the two-particle basis (4), we arrive at the effective moiré potential for excitons

$$\mathcal{H}_m(\mathbf{r}) = \begin{pmatrix} \mathcal{E}_X(\mathbf{r}) & 0 & \tilde{T}_c(\mathbf{r}) & -\tilde{T}_v(\mathbf{r}) \\ 0 & \mathcal{E}_X(\mathbf{r}) & -\tilde{T}_v(\mathbf{r}) & \tilde{T}_c(\mathbf{r}) \\ \tilde{T}_c(\mathbf{r}) & -\tilde{T}_v(\mathbf{r}) & \mathcal{E}_{IX}(\mathbf{r}) & 0 \\ -\tilde{T}_v(\mathbf{r}) & \tilde{T}_c(\mathbf{r}) & 0 & \mathcal{E}_{IX}(\mathbf{r}) \end{pmatrix}, \quad (6)$$

with the basis ordering $\{|X_b\rangle, |X_t\rangle, |IX_b^t\rangle, |IX_t^b\rangle\}$, and with tunneling functions \tilde{T}_α , renormalized by the overlap between X and IX RM wave functions. We have defined

$$\mathcal{E}_\mu(\mathbf{r}) = \mathcal{E}^{(0)} + \delta\epsilon_c(\mathbf{r}) - \delta\epsilon_v(\mathbf{r}) + \epsilon_\mu(\mathbf{r}), \quad (7)$$

containing the position-dependent conduction- and valence-band edge energies $\delta\epsilon_\alpha(\mathbf{r})$, and binding energy $\epsilon_\mu(\mathbf{r})$. Here, $\mathcal{E}^{(0)} = 2$ eV is the monolayer phosphorene band gap, extracted from *ab initio* calculations [42]. All terms in (6) are given explicitly in the Supplemental Material [29].

To visualize the effects of the moiré potential (6) on the exciton states (4), we have computed the lowest-energy eigenvalue of $\mathcal{H}_m(\mathbf{r})$ at each supercell position \mathbf{r} . The spatial variation of this eigenvalue represents an effective potential landscape [43] for otherwise free excitons propagating in the twisted phosphorene bilayer. Figure 2(c) shows that this potential landscape exhibits minima with approximate C_{2v} point symmetry at HH regions. Below, we show that these potential wells can localize excitons for small twist angles ($\theta < 4^\circ$), whereas at intermediate angles ($4^\circ < \theta \lesssim 10^\circ$) the excitons become delocalized exclusively along the \hat{y} , or armchair direction.

Exciton minibands. The total exciton Hamiltonian consists of (6), plus the exciton kinetic energy

$$H_K(\mathbf{Q}', \mathbf{Q}) = \delta_{\mathbf{Q}', \mathbf{Q}} \mathbb{1}_{4 \times 4} \frac{\hbar^2}{2} \mathbf{Q}'^T M_0^{-1} \mathbf{Q}, \quad (8)$$

with \mathbf{Q} the exciton c.m. wave vector, and $M_0^{-1} = \text{diag}([m_x^c + m_x^v]^{-1}, [m_y^c + m_y^v]^{-1})$ the exciton anisotropic inverse mass tensor ($m_x^c = 1.12m_0$, $m_y^c = 0.46m_0$, $m_x^v = 1.61m_0$ and $m_y^v = 0.23m_0$, with m_0 the free-electron mass). We have neglected layer-rotation effects on the inverse mass tensors, thus introducing two sources of error into our calculations: Firstly, a total error below 3% for both the X and IX c.m. dispersions, and for the IX RM energies, at twist angles within the range of validity of our model. Secondly, the appearance of a perturbation that couples the IX c.m. and RM degrees of freedom, much weaker than either the electron-hole interaction

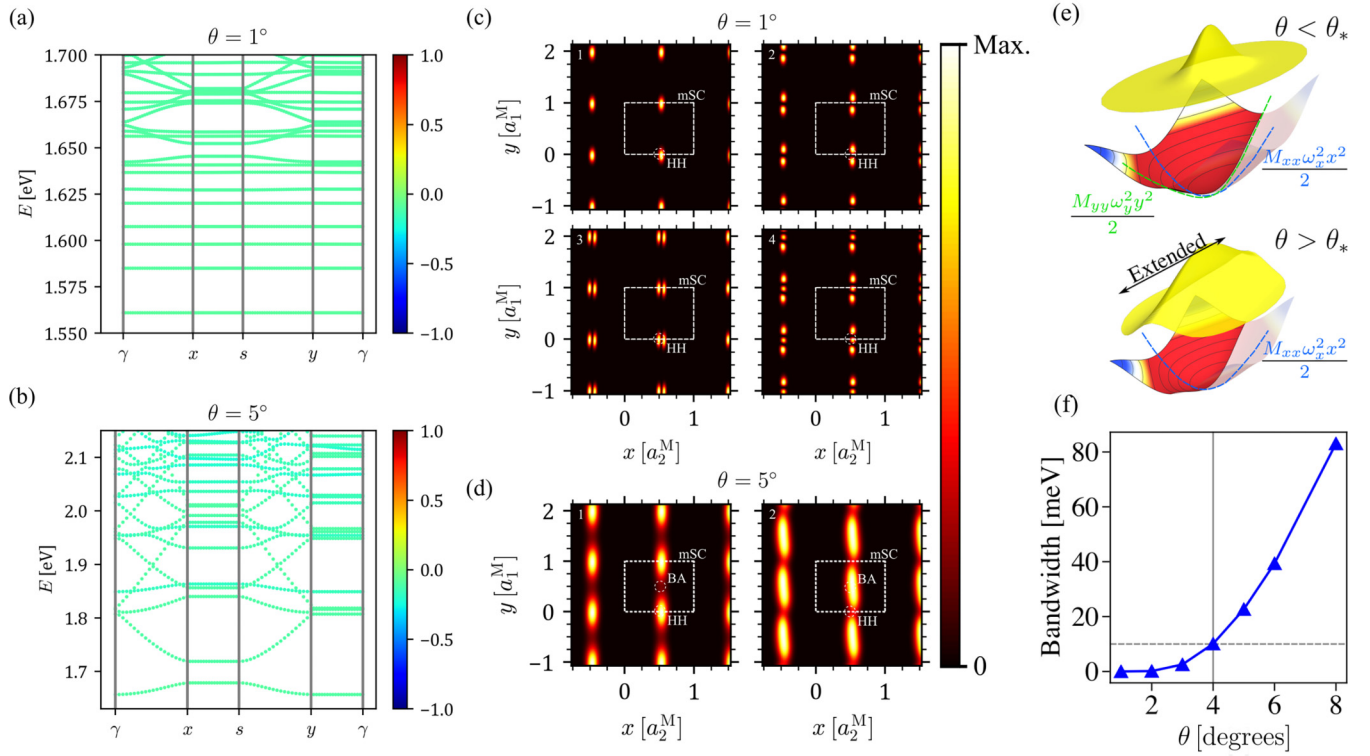


FIG. 3. (a) Exciton miniband structure for twisted phosphorene bilayers encapsulated in hBN with $\theta = 1^\circ$ and (b) $\theta = 5^\circ$. The band colors indicate the intra- and interlayer exciton contents of each eigenstate, with blue (red) corresponding to a pure X (IX) state, and green to a maximally mixed hX state. (c) Average spatial distributions of the first four excitonic minibands for $\theta = 1^\circ$ and (d) of the first two minibands for $\theta = 5^\circ$. (e) Illustration of the moiré potential wells and their lowest-energy states (offset for clarity), for $\theta < \theta_*$ and $\theta > \theta_*$. The approximating anisotropic harmonic oscillator potentials which confine the exciton are shown. (f) Lowest miniband width as a function of the twist angle. The $\theta_* = 4^\circ$ threshold between the 0D and 1D c.m. motion dimensionality regimes is indicated with a vertical line.

or the moiré potential, and which can be neglected as a first approximation [29]. In addition, we have neglected X dispersion nonanalyticities predicted [44] for momenta $\lesssim 0.03 \text{ \AA}^{-1}$, well below the smallest mBZ sizes studied in this Letter.

We numerically diagonalized the total Hamiltonian using a zone-folding approach [23]: The moiré potential (6) mixes any X basis function (4a) at wave vector \mathbf{Q} with any IX basis function (4b) at wave vector $\mathbf{Q}_{m,n} \equiv \mathbf{Q} + \mathbf{g}_{m,n}$. Taking $\mathbf{Q} \in \text{mBZ}$, all wave vectors $\mathbf{Q}_{m,n}$ can be “folded” onto the mBZ, and relabeled as states of momenta \mathbf{Q} belonging to a so-called miniband (m, n) . In this scheme, the effective model becomes an independent eigenvalue problem for every $\mathbf{Q} \in \text{mBZ}$, which we solved numerically for a large number of minibands. Convergence to within a 1 meV tolerance was obtained for the lowest few energy eigenvalues using a total of 2500 basis states.

Figures 3(a) and 3(b) show the moiré exciton miniband structures, computed for the representative twist angles $\theta = 1^\circ$ and 5° . For $\theta = 1^\circ$, the lowest few minibands are flat, corresponding to zero group velocity Bloch states. Intuition drawn from Fig. 2(c) suggests that these states form arrays of quantum-dot-like wave functions, localized at HH regions across the superlattice, with suppressed hopping between neighboring cells [11]. This is verified in Fig. 3(c), which shows the mBZ-averaged exciton densities of the first four minibands of Fig. 3(a). In each case, the localization region

coincides with the potential minima at HH regions of the mSC [Fig. 2(c)]. The formation of multiple flat bands shows that, at small twist angles such as $\theta = 1^\circ$, the moiré potential wells are deep and wide enough to host several localized states, with spatial distributions reminiscent of the first few levels of a harmonic oscillator elongated in the \hat{y} direction [29].

All moiré excitons computed with our model are linear superpositions of X and IX states. In Figs. 3(a) and 3(b), we have color-coded the X and IX contents of each state, with blue (red) representing a pure X (IX) state, and green representing a maximally mixed state, known as a hybrid exciton (hX) [23,45]. hXs are of wide interest for optoelectronics, as they combine the strong oscillator strength of X’s with the large electric dipole moment of IX’s, making them simultaneously optically active and susceptible to out-of-plane electric fields. Our results of Fig. 3(a) indicate that all low-energy moiré excitons in a $\theta = 1^\circ$ phosphorene bilayer are hX’s, and thus both bright and tunable.

One-dimensional moiré excitons. Figure 3(b) shows the computed miniband structure for $\theta = 5^\circ$, where the first few bands become dispersive in the \hat{y} direction, while remaining flat along the \hat{x} axis. This indicates moiré excitons delocalized in the former direction, but confined in the latter, representing a periodic array of quasi-1D states, reminiscent of quantum wires. To illustrate this, Fig. 3(d) shows the mBZ-averaged exciton densities of the first two minibands of Fig. 3(b). In

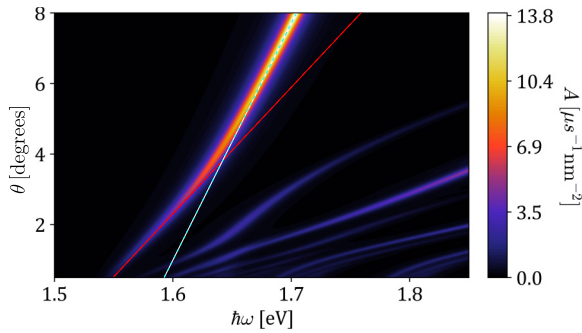


FIG. 4. Absorption spectra for light polarized along the \hat{x} (zigzag) direction for varying θ in hBN-encapsulated twisted phosphorene bilayers. The linear fit for the first absorption line is shown for the $\theta < 4^\circ$ regime (red) and for the $\theta > 4^\circ$ regime (blue).

addition, Fig. 3(b) also shows that all low-energy moiré excitons remain maximally mixed hX's at intermediate twist angles.

Delocalization along the \hat{y} direction is mainly a consequence of the lighter exciton mass in this direction ($M_{xx} = 2.73m_0$, $M_{yy} = 0.69m_0$). The mSC shrinks as the twist angle increases, resulting in progressively narrower potential wells that eventually become unable to confine the moiré excitons. This occurs first along the \hat{y} , or armchair axis, despite the larger width of the potential wells in that direction [Fig. 2(c)], due to the much lighter M_{yy} , as illustrated in Fig. 3(e). This is in stark contrast with the case of twisted TMD bilayers in the absence of uniaxial strain [46], where delocalization of moiré trapped excitons and carriers is fully isotropic [11,47].

To quantitatively describe the crossover between the zero-dimensional (0D) and 1D moiré exciton states, Fig. 3(f) shows the evolution of the lowest moiré exciton miniband width with twist angle. We propose a band width of 10 meV as an empirical threshold, below which a band can be considered flat, based on the typical energy broadenings observed in angle-resolved photoemission spectroscopy (ARPES) experiments [48,49]. The 0D-1D crossover angle θ_* can then be defined as the twist angle for which the lowest miniband width is 10 meV. We find that $\theta_* = 4^\circ$, well within the range of validity of our model. A subsequent 1D-2D crossover is expected at twist angles beyond the validity of our model [50].

Moiré optical signatures. We have found direct optical signatures of the 0D-1D crossover, experimentally accessible through optical absorption measurements. The optical selection rules for both intra- and interlayer excitons in the phosphorene bilayer [29] are identical to those of monolayer phosphorene [20,21,51,52]. Hence, all of our photoabsorption calculations correspond to linearly polarized light along the \hat{x} or zigzag direction of the phosphorene structure [Fig. 1(a)]. Figure 4 shows the evolution of the absorption spectrum of 1s excitons, as a function of twist angle. The presence of moiré excitons can be inferred at first glance by the presence of multiple absorption lines [45,53–55] at energies close to that of the monolayer X state. These lines correspond to γ -point hX's, and their oscillator strengths are dictated by the magnitude of their Γ -point X component in their wave functions.

Focusing on the two leftmost absorption lines in Fig. 4, we see that both blueshift linearly with increasing twist angle, before they exhibit a sudden decrease in slope, treating θ as the abscissa. Figure 4 shows that the twist angle at which the slope change occurs for the first absorption line coincides with our estimated dimensional crossover angle $\theta_* = 4^\circ$. For the second line, this occurs slightly below 2° .

The absorption-line twist angle dependence can be understood in terms of the dimensional crossover of the moiré exciton states. In the 0D regime, the moiré exciton energies are well approximated by the zero-point energy of the confining potential wells, as illustrated on the top of Fig. 3(f). Since the confining potential has approximately rectangular (C_{2v}) symmetry, the zero-point energy is separable into two components,

$$\frac{\hbar\omega_x(\theta)}{2} + \frac{\hbar\omega_y(\theta)}{2} = \left(\frac{\hbar\omega_x^0}{2} + \frac{\hbar\omega_y^0}{2} \right) + (\sigma_x + \sigma_y)\theta, \quad (9)$$

both of which increase linearly with slopes $\sigma_x, \sigma_y > 0$ as the twist angle grows and the potential wells narrow. Passing the threshold angle θ_* into the 1D regime, the zero-point energy component $\hbar\omega_x(\theta)/2$ is replaced by the kinetic energy along the armchair direction, which vanishes for the lowest γ -point state. The energy of the optically active 1D moiré exciton then varies with θ as $\sigma_y\theta$, with a reduced slope $\sigma_y < \sigma_x + \sigma_y$.

Conclusions. We have predicted a dimensional crossover for moiré exciton states in twisted phosphorene bilayers, from quantum-dot-like (0D) to quantum-wire-like (1D) arrays, at an experimentally accessible twist angle of $\theta_* = 4^\circ$. Our calculations show that the effective excitonic dimension can be identified experimentally by looking at the twist-angle dependence of the bilayer's optical absorption spectrum, which bears signatures of the dimensionality crossover. Further experimental evidence may be found through exciton diffusion measurements [56–60], where the extreme group velocity anisotropy may lead to unidirectional diffusion along the phosphorene armchair axis for twist angles above θ_* . We have established that the predicted dimensionality crossover is driven by the large anisotropies of the carrier dispersions in the monolayer material, magnified by the moiré potential. Therefore, we expect analogous effects in other anisotropic 2D semiconductors, such as the group-IV monochalcogenides. Whereas lateral confinement of 2D excitons has been reported in strained TMD-based systems [46,61], phosphorene offers a twist-angle controlled crossover into this 1D regime while retaining its equilibrium crystal structure. Our results highlight twisted bilayers of anisotropic 2D semiconductors as prime candidates for engineering versatile quantum many-body simulators, offering control over the system dimensionality.

Acknowledgments. I.S. acknowledges financial support from CONAHCyT (Mexico), through a Becas Nacionales graduate scholarship, as well as from the University of Manchester's Dean's Doctoral Scholarship. D.A.R.-T. acknowledges funding from PAPIIT-DGAPA-UNAM Grant No. IA106523, and CONAHCyT (Mexico) Grants No. A1-S-14407 and No. 1564464. The authors would like to thank J. Guerrero-Sánchez and F. Mireles for fruitful discussions at the beginning of this project.

- [1] D. M. Kennes, M. Claassen, L. Xian, A. Georges, A. J. Millis, J. Hone, C. R. Dean, D. N. Basov, A. N. Pasupathy, and A. Rubio, *Nat. Phys.* **17**, 155 (2021).
- [2] L. Wang, E.-M. Shih, A. Ghiotto, L. Xian, D. A. Rhodes, C. Tan, M. Claassen, D. M. Kennes, Y. Bai, B. Kim *et al.*, *Nat. Mater.* **19**, 861 (2020).
- [3] Y. Tang, L. Li, T. Li, Y. Xu, S. Liu, K. Barmak, K. Watanabe, T. Taniguchi, A. H. MacDonald, J. Shan *et al.*, *Nature (London)* **579**, 353 (2020).
- [4] H. Li, S. Li, E. C. Regan, D. Wang, W. Zhao, S. Kahn, K. Yumigeta, M. Blei, T. Taniguchi, K. Watanabe *et al.*, *Nature (London)* **597**, 650 (2021).
- [5] P. Wang, G. Yu, Y. H. Kwan, Y. Jia, S. Lei, S. Klemen, F. A. Cevallos, R. Singha, T. Devakul, K. Watanabe *et al.*, *Nature (London)* **605**, 57 (2022).
- [6] L. Ma, P. X. Nguyen, Z. Wang, Y. Zeng, K. Watanabe, T. Taniguchi, A. H. MacDonald, K. F. Mak, and J. Shan, *Nature (London)* **598**, 585 (2021).
- [7] J. Gu, L. Ma, S. Liu, K. Watanabe, T. Taniguchi, J. C. Hone, J. Shan, and K. F. Mak, *Nat. Phys.* **18**, 395 (2022).
- [8] Y. Zeng, Z. Xia, R. Dery, K. Watanabe, T. Taniguchi, J. Shan, and K. F. Mak, *Nat. Mater.* **22**, 175 (2023).
- [9] F. Wu, T. Lovorn, E. Tutuc, and A. H. MacDonald, *Phys. Rev. Lett.* **121**, 026402 (2018).
- [10] M. Angeli and A. H. MacDonald, *Proc. Natl. Acad. Sci. USA* **118**, e2021826118 (2021).
- [11] S. J. Magorrian, V. V. Enaldiev, V. Zolyomi, F. Ferreira, V. I. Fal'ko, and D. A. Ruiz-Tijerina, *Phys. Rev. B* **104**, 125440 (2021).
- [12] D. M. Kennes, L. Xian, M. Claassen, and A. Rubio, *Nat. Commun.* **11**, 1124 (2020).
- [13] M. Fujimoto and T. Kariyado, *Phys. Rev. B* **104**, 125427 (2021).
- [14] I. Soltero, J. Guerrero-Sánchez, F. Mireles, and D. A. Ruiz-Tijerina, *Phys. Rev. B* **105**, 235421 (2022).
- [15] T. Giamarchi, *Quantum Physics in One Dimension* (Clarendon, Oxford, 2003), Vol. 121.
- [16] H. Guo, X. Zhang, and G. Lu, *Sci. Adv.* **9**, eadi5404 (2023).
- [17] H. Yao, L. Pizzino, and T. Giamarchi, *SciPost Phys.* **15**, 050 (2023).
- [18] C. Li and W. Yao, *2D Mater.* **11**, 015006 (2023).
- [19] L. C. Gomes and A. Carvalho, *Phys. Rev. B* **92**, 085406 (2015).
- [20] J. Qiao, X. Kong, Z.-X. Hu, F. Yang, and W. Ji, *Nat. Commun.* **5**, 4475 (2014).
- [21] A. S. Rodin, A. Carvalho, and A. H. Castro Neto, *Phys. Rev. Lett.* **112**, 176801 (2014).
- [22] Y. Wang, Z. Wang, W. Yao, G.-B. Liu, and H. Yu, *Phys. Rev. B* **95**, 115429 (2017).
- [23] D. A. Ruiz-Tijerina and V. I. Fal'ko, *Phys. Rev. B* **99**, 125424 (2019).
- [24] W. Luo, D. Y. Zemlyanov, C. A. Milligan, Y. Du, L. Yang, Y. Wu, and P. D. Ye, *Nanotechnology* **27**, 434002 (2016).
- [25] T. Fang, T. Liu, Z. Jiang, R. Yang, P. Servati, and G. Xia, *ACS Appl. Nano Mater.* **2**, 3138 (2019).
- [26] S. Huang, G. Zhang, F. Fan, C. Song, F. Wang, Q. Xing, C. Wang, H. Wu, and H. Yan, *Nat. Commun.* **10**, 2447 (2019).
- [27] S. Zhao, E. Wang, E. A. Üzer, S. Guo, R. Qi, J. Tan, K. Watanabe, T. Taniguchi, T. Nilges, P. Gao *et al.*, *Nat. Commun.* **12**, 3947 (2021).
- [28] D. W. Boukhalov, S. Nappini, M. Vorokhta, T. O. Menteş, L. Piliari, M. Panahi, F. Genuzio, J. De Santis, C.-N. Kuo, C. S. Lue *et al.*, *Adv. Funct. Mater.* **31**, 2106228 (2021).
- [29] See Supplemental material at <http://link.aps.org/supplemental/10.1103/PhysRevB.108.L201401> for model and calculation details. See also Refs. [62–66] therein.
- [30] In a layered system, treating the simple type of anisotropy $\epsilon = \text{diag}(\epsilon_{\parallel}, \epsilon_{\parallel}, \epsilon_{\perp})$ reduces to redefining an effective isotropic dielectric constant $\tilde{\epsilon} = \sqrt{\epsilon_{\parallel}\epsilon_{\perp}}$, and rescaling the interlayer distance as $\tilde{d} = d\sqrt{\epsilon_{\parallel}/\epsilon_{\perp}}$; see Supplemental Material Note D in Ref. [29].
- [31] Our results for the spatial modulation of the exciton binding energies vary by less than 1meV if we choose the static values of the hBN dielectric tensor. See Supplemental Material Note G in Ref. [29].
- [32] R. Geick, C. H. Perry, and G. Rupprecht, *Phys. Rev.* **146**, 543 (1966).
- [33] A. Laturia, M. L. Van de Put, and W. G. Vandenberghe, *npj 2D Mater. Appl.* **2**, 6 (2018).
- [34] M. Danovich, D. A. Ruiz-Tijerina, R. J. Hunt, M. Szyniszewski, N. D. Drummond, and V. I. Fal'ko, *Phys. Rev. B* **97**, 195452 (2018).
- [35] J. J. S. Viner, L. P. McDonnell, D. A. Ruiz-Tijerina, P. Rivera, X. Xu, V. I. Fal'ko, and D. C. Smith, *2D Mater.* **8**, 035047 (2021).
- [36] J. C. G. Henriques and N. M. R. Peres, *Phys. Rev. B* **101**, 035406 (2020).
- [37] We have also considered the RM wave functions as adiabatically depending on the local stacking configuration: $X[\rho, \mathbf{r}_0(\mathbf{r})]$ and $Y[\rho, \mathbf{r}_0(\mathbf{r})]$. The \mathbf{r}_0 dependence of these functions introduces an additional spatial dependence to the matrix elements $\langle X_{\lambda', n'}(\mathbf{Q}) | H_{\text{exc}} | X_{\lambda, n}(\mathbf{Q}) \rangle$. We have numerically determined that this variation is $< 1\%$, and thus negligible.
- [38] J. J. Griffin and J. A. Wheeler, *Phys. Rev.* **108**, 311 (1957).
- [39] J. C. G. Henriques, G. B. Ventura, C. D. M. Fernandes, and N. M. R. Peres, *J. Phys.: Condens. Matter* **32**, 025304 (2020).
- [40] D. A. Ruiz-Tijerina, I. Soltero, and F. Mireles, *Phys. Rev. B* **102**, 195403 (2020).
- [41] The lowest X and IX states transform as the A_1 irreducible representation of the symmetry group C_{2v} of the RM Hamiltonian, and look like 1s hydrogenic states elongated in the y direction [29], justifying the label 1s. The eventual importance of, e.g., 2p or 2s excited states for the 1s moiré exciton band structures is determined by the 2p-2s and 2s-1s wave function overlaps, which we estimate to be at least one order of magnitude smaller than any 1s-1s overlap. Moreover, the oscillator strength of the 2s intralayer exciton is also estimated to be much weaker than that of its 1s counterpart, such that it can be neglected in the optical spectrum.
- [42] V. Tran, R. Soklaski, Y. Liang, and L. Yang, *Phys. Rev. B* **89**, 235319 (2014).
- [43] F. Ferreira, S. J. Magorrian, V. V. Enaldiev, D. A. Ruiz-Tijerina, and V. I. Fal'ko, *Appl. Phys. Lett.* **118**, 241602 (2021).
- [44] D. Y. Qiu, G. Cohen, D. Novichkova, and S. Refaely-Abramson, *Nano Lett.* **21**, 7644 (2021).
- [45] E. M. Alexeev, D. A. Ruiz-Tijerina, M. Danovich, M. J. Hamer, D. J. Terry, P. K. Nayak, S. Ahn, S. Pak, J. Lee, J. I. Sohn *et al.*, *Nature (London)* **567**, 81 (2019).
- [46] H. Zheng, D. Zhai, and W. Yao, *2D Mater.* **8**, 044016 (2021).

- [47] S. Brem, C. Linderälv, P. Erhart, and E. Malic, *Nano Lett.* **20**, 8534 (2020).
- [48] C. Q. Han, M. Y. Yao, X. X. Bai, L. Miao, F. Zhu, D. D. Guan, S. Wang, C. L. Gao, C. Liu, D. Qian, Y. Liu, and J.-F. Jia, *Phys. Rev. B* **90**, 085101 (2014).
- [49] F. Margot, S. Lisi, I. Cucchi, E. Cappelli, A. Hunter, I. Gutiérrez-Lezama, K. Ma, F. von Rohr, C. Berthod, F. Petocchi *et al.*, *Nano Lett.* **23**, 6433 (2023).
- [50] C. Sevik, J. R. Wallbank, O. Gülseren, F. M. Peeters, and D. Çakır, *2D Mater.* **4**, 035025 (2017).
- [51] P. Li and I. Appelbaum, *Phys. Rev. B* **90**, 115439 (2014).
- [52] A. Castellanos-Gomez, L. Vicarelli, E. Prada, J. O. Island, K. L. Narasimha-Acharya, S. I. Blanter, D. J. Groenendijk, M. Buscema, G. A. Steele, J. V. Alvarez *et al.*, *2D Mater.* **1**, 025001 (2014).
- [53] K. Tran, G. Moody, F. Wu, X. Lu, J. Choi, K. Kim, A. Rai, D. A. Sanchez, J. Quan, A. Singh *et al.*, *Nature (London)* **567**, 71 (2019).
- [54] C. Jin, E. C. Regan, A. Yan, M. Iqbal Bakti Utama, D. Wang, S. Zhao, Y. Qin, S. Yang, Z. Zheng, S. Shi *et al.*, *Nature (London)* **567**, 76 (2019).
- [55] K. L. Seyler, P. Rivera, H. Yu, N. P. Wilson, E. L. Ray, D. G. Mandrus, J. Yan, W. Yao, and X. Xu, *Nature (London)* **567**, 66 (2019).
- [56] J. Choi, W.-T. Hsu, L.-S. Lu, L. Sun, H.-Y. Cheng, M.-H. Lee, J. Quan, K. Tran, C.-Y. Wang, M. Staab *et al.*, *Sci. Adv.* **6**, eaba8866 (2020).
- [57] J. Wang, Q. Shi, E.-M. Shih, L. Zhou, W. Wu, Y. Bai, D. Rhodes, K. Barmak, J. Hone, C. R. Dean, and X.-Y. Zhu, *Phys. Rev. Lett.* **126**, 106804 (2021).
- [58] Z. Li, X. Lu, D. F. Cordovilla Leon, Z. Lyu, H. Xie, J. Hou, Y. Lu, X. Guo, A. Kaczmarek, T. Taniguchi *et al.*, *ACS Nano* **15**, 1539 (2021).
- [59] J. Choi, J. Embley, D. D. Blach, R. Perea-Causín, D. Erckensten, D. S. Kim, L. Yuan, W. Y. Yoon, T. Taniguchi, K. Watanabe *et al.*, *Nano Lett.* **23**, 4399 (2023).
- [60] A. Rossi, J. Zipfel, I. Maity, M. Lorenzon, L. Francaviglia, E. C. Regan, Z. Zhang, J. H. Nie, E. Barnard, K. Watanabe, T. Taniguchi, E. Rotenberg, F. Wang, J. Lischner, A. Raja, and A. Weber-Bargioni, [arXiv:2301.07750](https://arxiv.org/abs/2301.07750).
- [61] Y. Bai, L. Zhou, J. Wang, W. Wu, L. J. McGilly, D. Halbertal, C. F. B. Lo, F. Liu, J. Ardelean, P. Rivera *et al.*, *Nat. Mater.* **19**, 1068 (2020).
- [62] Q. Cai, D. Scullion, A. Falin, K. Watanabe, T. Taniguchi, Y. Chen, E. J. G. Santos, and L. H. Li, *Nanoscale* **9**, 3059 (2017).
- [63] P. E. Faria Junior, M. Kurpas, M. Gmitra, and J. Fabian, *Phys. Rev. B* **100**, 115203 (2019).
- [64] G. Kern, G. Kresse, and J. Hafner, *Phys. Rev. B* **59**, 8551 (1999).
- [65] K. H. Michel and B. Verberck, *Phys. Rev. B* **83**, 115328 (2011).
- [66] A. S. Rodin, A. Carvalho, and A. H. Castro Neto, *Phys. Rev. B* **90**, 075429 (2014).